Jin Han (Orcid ID: 0000-0002-6990-0280)
Zou Shasha (Orcid ID: 0000-0001-7726-2349)
Chen Gang (Orcid ID: 0000-0002-6690-4024)
Yan Chunxiao (Orcid ID: 0000-0002-6138-308X)
Zhang Shaodong (Orcid ID: 0000-0003-3345-1927)
Yang Guotao (Orcid ID: 0000-0002-4283-7111)

Formation and evolution of low-latitude F region field-aligned irregularities during the 7-8 September 2017 storm: Hainan coherent scatter phased array radar (HCOPAR) and Hainan digisonde observations

Han Jin[1,2], Shasha Zou[2], Gang Chen[1], Chunxiao Yan[1,3], Shaodong Zhang[1], Guotao Yang[3]

[1] Electronic Information School, Wuhan University, Wuhan, China.

[2] Department of Climate and Space Sciences and Engineering, University of Michigan, Ann Arbor, Michigan, USA

[3] National Space Science Center, Chinese Academy of Sciences, Beijing, China

Corresponding author: Han Jin (jinhan@whu.edu.cn)

Key Points

- Low-latitude ionospheric observations by 7-beam (east-west plane) VHF radar operated at Fuke, China and a nearby digisonde.

- Storm-induced PPEF is responsible for post-sunset FAIs and substorm-related over-shielding E-field leads to post-midnight FAIs.

- Plasma bubble irregularities showed dominantly westward drift rather than the eastward drift normally observed under quiet conditions.

Abstract

In this paper, we present a study of the low-latitude field-aligned irregularities formation and evolution during the 7-8 September 2017 geomagnetic storm by analyzing data of the very high frequency (VHF) coherent radar installed at Fuke, Hainan Island of China (19.5°N, 109.1°E; magnetic latitude 9.58°N) and a co-located Digisonde Portable Sounder. The prompt penetration of eastward interplanetary electric field associated with sudden southward turning of the interplanetary magnetic field (IMF) Bz resulted in large ascent of the F layer, making conducive conditions at the bottom-side of the layer for the growth of Rayleigh-Taylor (R-T) instability and the development of the plasma irregularities in the post-sunset hours. The irregularities persisted into the post-midnight sector when the southward IMF Bz gradually decreased to the quiet time values. In addition, the base height of F layer at Fuke also showed a large elevation after midnight during two consecutive substorm onsets, suggesting that the substorm-induced over-shielding penetration electric field may take over and modify the ambient zonal electric field in low-latitude ionosphere and induce the irregularities in the post-midnight sector. Moreover, different from the quiet time eastward movement of the irregularities observed over Fuke, the

storm-time irregularities displayed no zonal drift at the initial period and subsequently began drifting westward. The reversal of background plasma zonal drift velocity observed by Hainan digisonde is considered to be responsible for the storm-time zonal drift pattern of the irregularities.

1 Introduction

The equatorial/low-latitude F region field-aligned irregularities (FAIs), also known as equatorial/low-latitude spread F, have been extensively studied for decades by using various instruments, such as VHF radars [e.g. Woodman and LaHoz, 1976; Tsunoda, 1980; Yokoyama and Fukao, 2006; Li et al., 2013], ionosondes [Abdu et al., 2003; Lee et al, 2005; Chen et al., 2006], optical airglow imager [Otsuka et al., 2004; Sobral et al. 2009; Hickey et al. 2015], GPS scintillation measurements [Pi et al., 1997; Li et al., 2010] and in situ satellites [Basu et al., 2001; Burke et al., 2004; Huang et al., 2012]. Plasma irregularities in the ionosphere may cause rapid variations in phase and amplitude of radio signals and lead to detrimental effect on navigation and communication system [Woodman, 2009, and references therein]. Therefore, it is important to understand the underlying generation mechanism of these ionospheric irregular structures.

The seasonal, longitudinal and solar-cycle dependence of the equatorial/low-latitude FAIs occurrences have been intensively investigated [e.g. Rastogi, 1980; Kil and Heelis, 1998; Burke

et al., 2004; Huang et al., 2014], but the day-to-day and storm-time variability of the FAIs occurrences is still a challenging problem for the forecast of equatorial/low-latitude spread F. It has been generally accepted that ionospheric irregularities are mainly generated via the generalized R-T instability [Ott, 1978] that may develop at the bottom-side of the F layer and rapidly arise to the topside ionosphere. The equatorial/low-latitude FAIs usually occur during post-sunset hours due to the evening pre-reversal enhancement (PRE) of zonal (eastward) electric field/vertical plasma drift [Woodman et al., 1970], which provides favorable conditions for the growth of the R-T instability by lifting the lower F layer to higher altitudes where the ion-neutral collision frequency is lower. The PRE of zonal electric field/vertical plasma drift is one of the most important factors for facilitating quiet time FAIs generation, but during storm time, other factors can also lead to perturbation in zonal electric field and thus facilitate the generation of FAIs.

The generation or suppression of equatorial/low-latitude FAIs during geomagnetic disturbances, in particular, geomagnetic storms, are very complicated and have been studied extensively [Martinis et al., 2005; Abdu, 2012 and references there in]. Under geomagnetic disturbance conditions, the equatorial/low-latitude zonal electric field, which controls the occurrence of FAIs, might be modified by two important drivers, i.e., prompt penetration of electric field (PPEF) from high-latitude to low-latitude/equatorial regions [Nishida, 1968] and disturbance dynamo

electric field (DDEF) driven by disturbed global thermospheric circulation due to Joule heating [Blanc and Richmond, 1980].

The equatorward penetration of dawn-dusk electric field (PPEF) occurs almost simultaneously with the sudden southward excursion of the interplanetary magnetic field (IMF) Bz and produce short-term (tens of minutes to 1-2h) perturbations in the equatorial/low-latitude zonal electric field. The PPEF is eastward (westward) on the day (night) side which has the same polarity with the quiet time ambient zonal electric field at equatorial/low-latitude ionosphere. The eastward PPEF superposed on the normal PRE of zonal electric field in evening hours will enhance the vertical plasma drift in F region, consequently inducing the equatorial/low-latitude FAIs generation. Shielding electric field gradually builds up in the inner magnetosphere region after the enhanced convection, and the PPEF will be gradually shielded [Kikuchi et al., 2008]. However, the IMF Bz usually fluctuates and therefore, the equatorial electric field is rarely balanced. If there is a sudden IMF Bz northward turning or a substorm onset, the PPEF will reduce and the shielding electric field may dominate and the total electric field may now become dusk-to-dawn, i.e. westward (eastward) on the day (night) side, which is opposite of the dawn-dusk PPEF [Fujita et al., 2010; Kikuchi et al., 2003; Wei et al., 2009; Hashimoto et al., 2011]. On the other hand, the DDEF occurs with a few hours of delay from the beginning of the storm and usually lasts for longer period than the PPEF. In general, the DDEF has westward polarity in the evening hours and can diminish or even reverse the normal PRE of zonal electric field in

equatorial/low-latitude ionosphere, which then inhibit the development of the FAIs. Therefore, the excitation or inhibition of equatorial/low-latitude FAIs during the geomagnetic storm depends on the interplay between PPEF and DDEF. For instance, generation of FAIs during the main phase of the geomagnetic storm due to eastward PPEF in the dusk sector have been reported [i.e., Basu et al., 2001; Abdu et al., 2003; Tulasi Ram et al., 2008; Patra el al., 2016]. Abdu et al. [1997] reported the inhibition of the equatorial PRE and the post-sunset spread F due to the westward DDEF in the evening during the storm recovery. Recently, the inhibition of the irregularities over Taiwan during the 2015 St. Patrick's Day storm was studied by Rajesh et al. [2017] and was attributed to the westward over-shielding electric field resulting from transient northward turning of IMF Bz around the dusk.

The suppression or initiation of the equatorial/low-latitude FAIs during the geomagnetic storm largely hinges on the competitive effects of these perturbation electric fields mentioned above. In this paper, we investigate the development of the low-latitude ionospheric zonal electric field and irregularities during the 7-8 September 2017 storm. Our observations are primarily based on the VHF coherent radar and the digisonde installed at Fuke, Hainan Island of China (19.5°N, 109.1°E; magnetic latitude 9.58°N). A brief description of the instruments is presented in Section 2. In Section 3, we briefly introduce the characteristics of the 7-8 September 2017 geomagnetic storm, and then present the low-latitude ionospheric irregularities as well as the background plasma condition during the storm. Sections 4 and 5 give the discussion and conclusion,

respectively. The results we present here contribute to improve current understanding of the storm-time low latitude plasma irregularities generation and evolution.

2 Instruments

Figure 1 shows the location and field-of-view of the Hainan coherent scatter phased array radar (HCOPAR) located at Fuke, Hainan Island of China (19.5°N, 109.1°E; magnetic latitude 9.58°N). It is one of the most important radio systems of Chinese Meridian Project [Wang, 2010]. It operates at 47 MHz with 54 kW peak power and 2 MHz bandwidth to detect the 3.2 m scale field-aligned irregularities in the low-latitude ionosphere [Chen et al., 2017]. Its antenna array is consisted of 18×4 five-element linear-polarized Yagi antennas covering an area of 2000 m^2. As shown in Figure 1, the HCOPAR has an active phased array system, which allows the radar beam to steer in seven directions, each separated by 7.5° in azimuth ranging from 22.5° (beam 1) to -22.5° (beam 7) around the geographic north. The central beam (beam 4) of the radar points to the geographic north, which deviates from geomagnetic north only by 1°. The azimuth and elevation angles of the seven beams are (-22.5°, 59.72°), (-15°, 60.70°), (-7.5°, 61.24°), (0°, 61.36°), (7.5°, 61.06°), (15°, 60.35°) and (22.5°, 59.15°). The central direction of the seven radar beams is almost perpendicular to the local geomagnetic field at altitudes of the ionospheric E and F regions to ensure the simultaneous observations of E and F region field-aligned irregularities. The range resolution of the radar measurement is 0.711 km. The arrangement of

the seven radar beams provides a view of two-dimensional structures of the backscatter echoes. The time duration to complete one azimuth scan from beam 1 to beam 7 is approximately 120 s. The fan sector maps can be constructed every 2 minutes by combining the signal-to-noise ratio from seven beams, revealing the spatial and temporal evolutions of the ionospheric irregularities.

The background ionospheric condition and drifts are recorded by a co-located Digisonde Portable Sounder (DPS-4D) [Reinisch et al., 2009] at Hainan. The Hainan digisonde routinely operates every 15 minutes to obtain an ionogram and it was operated every 5 minutes to obtain an ionogram during the storm days. The virtual height of the bottom-side F layer, h'F, can be manually scaled from an ionogram. The mean vertical and zonal drift velocities in the F region can be calculated from Doppler skymap according to the angle of arrival and Doppler velocity of the echoes [Reinisch et al., 1998].

3 Observations

3.1 Characteristics of the 7-8 September 2017 Double Dip Storm

Figures 2a-f present the 1 min resolution data of solar wind velocity, density, dynamic pressure, IMF Bz, interplanetary electric field IEF Ey, and the symmetric index (SYM/H), respectively, during 7-8 September 2017. The data are obtained from the OMNI Web site, and they have been corrected for the propagation delay up to the Earth's bow shock. This geomagnetic storm was caused by multiple interplanetary coronal mass ejections (ICMEs), including a shocked-ICME

[Shen et al., 2017]. The IEF Ey component is calculated as Ey= -Vsw×Bz, where Vsw is the sunward solar wind velocity component. Sharp enhancements in the solar wind velocity, density and dynamic pressure were observed at around 23:11 UT on 7 September 2017, indicating the arrival of an interplanetary shock. The main phase of the storm commenced at ~23:31 UT on 7 September 2017 with a steep southward excursion of the IMF Bz component to -31.2 nT and the IEF Ey component reached ~21 mV/m. The first dip of the geomagnetic storm with the minimum SYM/H of -146 nT occurred at ~01:10 UT on 8 September 2017. The IMF Bz remained southward for more than 2 hours, became northward at ~02:30 UT 8 September and remained northward for ~9 hours except for five transient southward turnings. Another large and rapid IMF Bz southward turning occurred at 11:55 UT, reaching ~-17.4 nT and the IEF Ey component became eastward rapidly to the peak value of 13.76 mV/m. This second large southward turning of IMF Bz leads to the second main phase of the storm and another dip with SYM/H index reaching ~-115 nT. We focus on observations obtained during the second main phase when it was night time over our observing locations.

3.2 Ionospheric Irregularities and Background Condition During the Storm

Figure 3 shows the virtual height (h'F) variations of bottom-side F layer, vertical drift velocity and east (positive)-west (negative) drift velocity in the ionospheric F region obtained from the Hainan digisonde during 10:00-19:00 UT on 7 (blue) and 8 (red) September 2017. Because the storm initiated later than 19 UT on 7 September 2017, the period up to this time can be

considered as quiet time for comparison with storm time conditions. It is clear that the bottom-side F layer went up significantly, i.e., by 150 km (marked with arrow a), after ~11:40 UT on 8 September, i.e., right after the second IMF Bz southward turning, and reached a peak height of 387 km at ~12:35 UT in Figure 3a. Two more obvious ascending motions were observed during 13:50-14:20 UT and 17:00-17:45 UT (marked with arrow b and c, respectively). It is worth mentioning that the third uplifting of the bottom-side F layer occurred after local midnight, which will be discussed in more detail in the next section in terms of the cause of perturbation electric field in post-midnight sector. During the three episodes of the F layer uplift due to positive vertical flow, shown in Figure 3b, the peak vertical drift velocity reached values of 145.8 m/s, 169.7 m/s and 121.8 m/s, respectively. As shown in Figure 3c, the zonal drift velocity was steadily negative, i.e., westward varying from about -16 m/s to -200 m/s on 8 September after ~ 12:45 UT, before which the zonal drift of the background plasma fluctuated between eastward and westward. In contrast, the night time zonal drift of the background plasma on 7 September was mostly eastward.

The altitude-time variations of signal-to-noise ratio (SNR) and line-of-sight Doppler velocity of the FAIs observed on 8 September 2017 by beam 4 of the HCOPAR are presented in Figure 4a and 4b, respectively. As shown in Figure 4a, seven groups of FAIs echoes were observed and are labeled from A to G. A small echo (labeled with A) started to emerge at ~12:37 UT (LT=UT+7.3h) at altitudes from 330 km to 370 km. Then an upwelling plume-like structure of

the FAIs echoes (labeled with B) appeared at ~13:15 UT with durations of about 80 min, covering the altitudes from 305 km to 460 km. At ~13:47 UT, another upwelling plume-like structure of the FAIs echoes (labeled with C) was observed at higher altitudes from 510 km to 590 km and the echo intensity was much weaker than group B. Plumes in group D started at ~14:57 UT at altitudes from 360 km to 560 km with durations of about 15 min. Group E of the FAIs echoes followed closely with stronger intensity and lower altitude ranges than group D. Around midnight, group F of the FAIs echoes appeared at around 400 km and showed descending pattern over time. During post-midnight hours, the HCOPAR still recorded a strip-like structure of FAIs echoes (labeled with G). Group G of the FAIs echoes initiated at ~17:15 UT at altitude of ~540 km and displayed similar descending pattern as group F. Because beam 4 of the HCOPAR is basically measuring within a magnetic meridional plane, the line-of-sight Doppler velocity measured along beam 4 purely represents meridional (northward and upward or southward and downward) movement, rather than a combination of zonal and meridional velocity components of FAIs drift. As displayed in Figure 4b, the line-of-sight Doppler velocities of the post-sunset FAIs echoes were mainly positive (varying from ~20 m/s to ~100 m/s) except for the narrow descending structures in group B, indicating that the majority of the FAIs was moving away (northward and upward) from the radar. The large upward velocities of the upwelling plume structures suggested that these FAIs were still in growth phase. The Doppler velocity of post-midnight group G was mostly negative (-20 to -2 m/s), suggesting the irregularity was moving toward (southward and downward) the radar.

In order to investigate the spatial distribution and the zonal drift direction of the FAIs, the altitude-time-SNR plots of the FAIs echoes observed in different beam directions (from beam1 to beam7) are displayed from top to bottom in Figure 5a-g. Considering the different formation location (i.e. inside or outside of the radar beams) of the FAIs echoes, they can be divided into two types, type-1 (group A, B, E in Figure 4a) and type-2 (group C, D, F, G in Figure 4a). Type-1 echoes were freshly generated within the field of view (FoV) of the HCOPAR and were still in their growth phase. Type-2 echoes were generated elsewhere and then drifting into the FoV of the HCOPAR. Type-2 FAIs echoes in this case were mostly in decaying phase, because the echo intensity became weaker when moving across the radar beams. The zonal movement of the FAIs in beams 5-7 during 12:45-13:20 UT was not clear, but the other FAIs echoes exhibited obvious westward drift, appearing firstly in the easternmost beams and later in western beams. This westward moving feature is different from the typical post-sunset eastward movement observed by HCOPAR over the past few years (see for example, Figure 11 in Chen et al., 2017). This is consistent with the westward drifting of the background plasma after ~ 12:45 UT observed in Figure 3c. The zonally motionless FAIs echoes occurred during the period of eastward wind or nearly zero zonal wind.

To illustrate the spatial distribution of the irregularities, we projected the FAIs echo intensity from different beams onto the zonal-vertical plane to generate the fan sector maps by using two-

dimension interpolation method. The time sequence of two-dimensional fan sector maps of FAIs echo SNR from 13:09 UT to 14:45 UT on 8 September displayed in Figure 6 provides us a good view of the freshly generated type of the FAIs, i.e., type-1 (group B in Figure 4a). An echo appeared in the central FoV of HCOPAR at 13:21 UT at the altitudes from 320 km to 356 km, and then it expanded to higher altitudes with increasing echo intensity. Meanwhile, the fan sector maps show a clear westward movement of the FAIs echoes. These maps have been used to help the classification of the FAIs types.

4 Discussion

4.1 Post-sunset FAIs

In previous section, we have presented our observations of the FAIs in the low-latitude ionospheric F region recorded by HCOPAR during the second main phase of the geomagnetic storm on 7-8 September 2017. As shown in Figure 2, the IEF Ey turned eastward due to the second large sudden southward turning of IMF Bz at 11:35 UT on 8 September 2017. Right after that, the base height of the F layer at Fuke started ascending rapidly and reached to a peak altitude of ~387 km, which was remarkably higher compared to its typical quiet day enhancement during post-sunset hours on 7 September. Subsequently, the F region FAIs started to emerge just a few minutes later than the time of peak uplift of h'F at Fuke as indicated in Figure 3a. The substantial upward movement of bottom-side F layer generated favorable

conditions for the growth of the R-T instability, which is believed to play an important role in inducing low-latitude plasma irregularities [Heelis, 2004 and references there in]. This sudden uplift of bottom-side F layer provides evidence for an enhancement of eastward electric field at Fuke and the timing of the eastward electric field enhancement agrees very well with the IEF increase based on the solar wind and IMF measurements. Therefore, we conclude that the strong eastward IEF penetrated to low-latitude ionosphere, uplifted the bottom-side F layer to higher altitudes and triggered the post-sunset FAIs. Aa et al. [2018] studied the widely-extended plasma bubbles over China during the same storm on 7-8 September 2017 by using data from Global Navigation Satellite System (GNSS) networks. The TEC depletion was observed after 12:45 UT, consistent with the FAIs observed by the HCOPAR.

During the recovery phase of the geomagnetic storm, the post-sunset equatorial plasma bubble is usually suppressed by over-shielding westward electric field [Abdu et al., 2009], which can cause downward plasma drift and reduce the growth rate of R-T instability. Besides over-shielding electric field, disturbance wind dynamo electric field can also suppress the irregularities in the recovery phase. However, the observations described in the previous section indicate that irregularities can still be triggered even in the recovery phase of the storm, if an additional storm intensification accompanied IMF southward turning and penetration of eastward IEF to low-latitude occur in the dusk sector.

4.2 Post-midnight FAIs

Under quiet condition, the ambient zonal electric field is usually westward in the post-midnight period and can cause downward plasma drift, so it does not support the FAIs generation after local midnight. In this case, the irregularities persisted into the post-midnight sector when the southward IMF Bz gradually recovered to its quiet time values. As displayed in Figure 5e-g, the FAIs emerged above 400km (highlighted with red circles) were freshly generated in beam 5 of HCOPAR after 16:15 UT and then drifted westward to beam 6 and 7 with increasing echo intensity. These FAIs were type-1 echoes and were still in growth phase. Figure 3a shows that the base height of F layer again started to lift at ~ 17:00 UT and reached a peak height of ~390 km at ~17:40 UT. During this period of bottom-side F layer elevation, the strip-like FAIs (group G in Figure 4a) were firstly recorded by beam 1 of the radar, continuing to drift westward and being recorded by the other beams successively. These echoes were type-2 echoes which were generated outside of the radar beams and they remained in the FoV of HCOPAR for about one hour from ~17:00 to ~18:00 UT. Both the uplift of F layer and irregularities occurring after midnight serve as direct evidences for high-latitude electric field penetrating to low-latitude ionosphere. As we discussed in the introduction section, under-shielding PPEF has eastward (westward) polarity on the day (night) side and over-shielding PPEF has westward (eastward) polarity on the day (night) side. Therefore, eastward over-shielding PPEF should be responsible for the uplift of F layer and subsequent irregularities in the post-midnight sector in this case.

Previous studies have demonstrated that over-shielding electric field can not only be triggered by IMF Bz northward turning [Fujita el al., 2010], but also by a substorm onset [e.g., Kikuchi et al., 2003; Wei et al., 2009; Hashimoto et al., 2011]. To investigate the possible cause of the over-shielding PPEF after midnight, we present the zoomed-in IMF Bz, the auroral activity indices, i.e., the AU/AL and AE indices, and the H component measured by two high-latitude magnetometers at Dikson, Russia (73.53°N, 80.70°E, magnetic latitude 69.04°N) and Tiksi, Russia (71.59°N,128.92°E; magnetic latitude 66.41°N) during 09:00-24:00 UT on 8 September in Figure 7a, 7b, 7c, 7d and 7e, respectively. We looked at the magnetometers that are used to construct the THEMIS real-time AE and selected the H component data from Dikson and Tiksi stations. The H component measured at these two stations showed the sharpest decrease, suggesting that they were closest to the substorm onset location and thus can better determine the accurate timing of substorm onset. As shown in Figure 7a, the IMF Bz exhibited northward excursion (marked by a blue arrow) during a short time period, which may cause eastward over-shielding electric field on the night side. However, the effect of the IMF Bz northward turning is expected to show up very quickly (a few minutes after the northward turning) instead of delaying for ~30-40 minutes. Therefore, it is likely that the small bump of base height of F layer (labeled with black arrow d) in Figure 3a was the result of over-shielding electric field due to the IMF Bz sudden but short northward turning. Another factor should be responsible for the uplift of F layer after 17:00 UT. As displayed in Figure 7b and 7c, the AL and AE indices indicated that there were several substorm expansions with the AE index exceeding 1000 nT after 16 UT. It is

obvious in Figure 7d and 7e that there were two sharp decreases of H component (marked by red arrows) between 16:00-18:00 UT, suggesting two consecutive substorm onsets while the IMF Bz was gradually decreasing/recovering towards quiet time values. Therefore, the large uplift of F layer after 17:00 UT is likely resulted from over-shielding PPEF, which was induced by substorm onset at ~17 UT. Wei et al. [2009] and Hashimoto et al. [2011] demonstrated that the over-shielding electric field can be quickly established after a substorm onset even without the IMF Bz northward turning. Simulation results based on the Rice Convection Model (RCM) also demonstrated that the over-shielding electric field can be set up right after substorm onset [Zhang et al., 2009]. Comparing with the post-sunset echoes, the intensity of the post-midnight echoes was much weaker. This may be attributed to the much lower vertical density gradient in the post-midnight sector [Huba and Joyce, 2010], so the growth rate of the R-T instability is much lower in post-midnight period than that during the post-sunset hours. Consequently, the post-midnight FAIs could not grow into strong upwelling plume structure like the post-sunset ones.

In addition, a distinct feature of the storm-time irregularities observed on 8 September at Fuke is that their zonal drift was westward except for the beginning period of the observation, which differs from the quiet time eastward velocities. Numerous studies [e.g. Yokoyama et al., 2004; Patra et al., 2014] have shown that the zonal drift of the nighttime plasma irregularities is eastward under quiet conditions. During magnetically disturbed conditions, the zonal velocities of plasma irregularities may slow down and/ or even reverse to westward [Abdu et al., 2003; Ma

and Maruyama, 2006; Basu et al., 2010; Patra et al., 2016]. In general, the zonal motion of the irregularities follows that of the ambient plasma. As seen in Figure 3c, the zonal drift of the background plasma fluctuated between westward and eastward in the initial hours and it reversed from eastward to stable westward at ~12:45 UT. The irregularities observed by the HCOPAR initiated at ~12:45 UT and represented little or even no zonal drift at the beginning of the observation as shown in Figure 5d-g. Subsequently, the irregularities traveled westward, moving together with the ambient plasma. Therefore, the irregularities zonal motion pattern described above can be attributed to the reversal of the background plasma zonal drift. Ma and Maruyama (2006) reported that a storm-induced super plasma bubble exhibited a much slower eastward drift velocity in contrast to the quiet time, and they attributed the slow eastward drift to the storm-time westward zonal wind. Reversal of zonal drift of the storm-time irregularities form large eastward to westward due to the disturbance dynamo effect was also studied by Patra et al. (2016). The westward turning of zonal drift velocities of the FAIs in our observation probably resulted from the storm-related thermospheric disturbance winds that have a strong westward component in low-latitude regions. Further studies are required to be conducted in terms of the storm-time thermospheric disturbance winds effects in future work.

5 Conclusion

In this study, the low-latitude ionospheric irregularities formation and evolution in response to the 7-8 September 2017 geomagnetic storm have been analyzed using data from HCOPAR and

Hainan digisonde. The second sudden southward turning of IMF Bz that caused intensification of the storm (in the recovery phase) resulted in prompt penetration of eastward IEF to low-latitude that enhanced the ambient zonal eastward electric field during post-sunset sector resulting in the uplift of the F layer to higher altitudes, creating favorable conditions for the growth of R-T instability and the generation of the FAIs in the post-sunset hours. Moreover, the elevation of base height of F layer recorded by the Hainan digisonde in the post-midnight sector and the post-midnight irregularities observed by HCOPAR are likely due to the substorm-related over-shielding electric field, which has eastward polarity on the night side. The zonal drift of the FAIs that usually follows the ambient plasma drift (normally eastward at night), was found to be near zero in the beginning and soon turned westward. The reversal of the background plasma zonal drift observed by Hainan digisonde is likely responsible to the unusual zonal drift pattern of storm-time irregularities.

Acknowledge

thank Arctic and Antarctic Research Institute (AARI), Department of Geophysics (http://geophys.aari.ru) for use of the AARI magnetometers data.

References

Aa, E., W. Huang, S. Liu, A. J. Ridley, S. Zou, L. Shi, Y. Chen, H. Shen, T. Yuan, J. Li and T. Wang (2018), Mid-latitude plasma bubble over China and adjacent areas during a magnetic storm on 08 September 2017, Space Weather, 16, doi:10.1002/2017SW001766.

Abdu, M. A., M. A. Sastri, J. MacDougall, I. S. Batista, and J. H. A. Sobral (1997), Equatorial disturbance dynamo electric field, longitudinal structure and spread F: A case study from GUARA/EITS campaigns, Geophys. Res. Lett., 24, 1707 – 1710.

Abdu, M. A., I. S. Batista, H. Takahashi, J. MacDougall, J. H. Sobral, A. F. Medeiros, and N. B. Trivedi (2003), Magnetospheric disturbance induced equatorial plasma bubble development and dynamics: A case study in Brazilian sector, J. Geophys. Res., 108(A12), 1449, doi:10.1029/2002JA009721.

Abdu, M. A., E. A. Kherani, I. S. Batista, and J. H. A. Sobral (2009), Equatorial evening prereversal vertical drift and spread F suppression by disturbance penetration electric fields, Geophys. Res. Lett., 36, L19103, doi:10.1029/2009GL039919.

Abdu, M. A. (2012). Equatorial spread F/plasma bubble irregularities under storm time disturbance electric fields. Journal of Atmospheric and Solar-Terrestrial Physics, 75, 44-56.

Basu, S., S. Basu, K. M. Groves, H. C. Yeh, S. Y. Su, F. J. Rich, P. J. Sultan, and M. J. Keskinen (2001), Response of the equatorial ionosphere in the South Atlantic region to the great magnetic storm of July 15, 2000, Geophys. Res. Lett., 28, 3577–3580, doi:10.1029/2001GL013259.

Basu, S., Su. Basu, E. MacKenzie, C. Bridgwood, C. E. Valladares, K. M. Groves, and C. Carrano (2010), Specification of the occurrence of equatorial ionospheric scintillations during the main phase of large magnetic storms within solar cycle 23, Radio Sci., 45, RS5009, doi:10.1029/2009RS004343.

Blanc, M., and A. D. Richmond (1980), The ionospheric disturbance dynamo, J. Geophys. Res., 85, 1669–1688, doi:10.1029/JA085iA04p01669.

Burke, W. J., L. C. Gentile, C. Y. Huang, C. E. Valladares, and S. Y. Su (2004), Longitudinal variability of equatorial plasma bubbles observed by DMSP and ROCSAT-1, J. Geophys. Res., 109, A12301, doi:10.1029/2004JA010583.

Chen, W. S., C. C. Lee, J. Y. Liu, F. D. Chu, and B. W. Reinisch (2006), Digisonde spread F and GPS phase fluctuations in the equatorial ionosphere during solar maximum, J. Geophys. Res., 111, A12305, doi:10.1029/2006JA011688.

Chen, G., H. Jin, J. Yan, X. Cui, S. Zhang, C. Yan, G. Yang, A. Lan, W. Gong, L. Qiao, C. Wu, and J. Wang (2017), Hainan Coherent Scatter Phased Array Radar (HCOPAR): System

Design and Ionospheric Irregularity Observations, IEEE Transactions on Geoscience and Remote Sensing, 55(8), 4757-4765.

Fujita, S., T. Kikuchi, and T. Tanaka (2010), State transition of the magnetosphere-ionosphere compound system due to a northward turn of the interplanetary magnetic field revealed from a global magnetohydrodynamic simulation and formation of the overshielding potential, J. Geophys. Res., 115, A11210, doi:10.1029/2010JA015550.

Hashimoto, K. K., T. Kikuchi, S. Watari, and M. A. Abdu (2011), Polar-equatorial ionospheric currents driven by the region 2 field-aligned currents at the onset of substorms, J. Geophys. Res., 116, A0921 7, doi:10.1029/2011JA016442.

Heelis, R. A. (2004). Electrodynamics in the low and middle latitude ionosphere: A tutorial. Journal of Atmospheric and Solar-Terrestrial Physics, 66(10), 825-838.

Hickey, D. A., C. R. Martinis, F. S. Rodrigues, R. H. Varney, M. A. Milla, M. J. Nicolls, A. Strømme, and J. F. Arratia (2015), Concurrent observations at the magnetic equator of small-scale irregularities and large-scale depletions associated with equatorial spread F, J. Geophys. Res. Space Physics, 120, 10,883–10,896, doi:10.1002/2015JA021991.

Huang, C.-S., O. de La Beaujardiere, P. A. Roddy, D. E. Hunton, J. O. Ballenthin, and M. R. Hairston (2012), Generation and characteristics of equatorial plasma bubbles detected by the C/NOFS satellite near the sunset terminator, J. Geophys. Res., 117, A11313, doi:10.1029/2012JA018163.

Huang, C.-S., O. de La Beaujardiere, P. A. Roddy, D. E. Hunton, J. Y. Liu, and S. P. Chen (2014), Occurrence probability and amplitude of equatorial ionospheric irregularities associated with plasma bubbles during low and moderate solar activities (2008–2012), J. Geophys. Res. Space Physics, 119, 1186–1199, doi:10.1002/2013JA019212.

Huba, J. D., and G. Joyce (2010), Global modeling of equatorial plasma bubbles, Geophys. Res. Lett., 37, L17104, doi:10.1029/2010GL044281.

Kil, H., and R. A. Heelis (1998), Global distribution of density irregularities in the equatorial ionosphere, J. Geophys. Res., 103(A1), 407–417, doi:10.1029/97JA02698.

Kikuchi, T., K. K. Hashimoto, T.-I. Kitamura, H. Tachihara, and B. Fejer (2003), Equatorial counterelectrojets during substorms, J. Geophys. Res., 108(A11), 1406, doi:10.1029/2003JA009915.

Kikuchi, T., K. K. Hashimoto, and K. Nozaki (2008), Penetration of magnetospheric electric fields to the equator during a geomagnetic storm, J. Geophys. Res., 113, A06214, doi:10.1029/2007JA012628.

Lee, C. C., J. Y. Liu, B. W. Reinisch, W. S. Chen, and F. D. Chu (2005), The effects of the pre-reversal ExB drift, the EIA asymmetry, and magnetic activity on the equatorial spread F during solar maximum, Ann. Geophys., 23, 745–751.

Li, G., et al. (2010), Longitudinal development of low-latitude ionospheric irregularities during the geomagnetic storms of July 2004, J. Geophys. Res., 115, A04304, doi:10.1029/2009JA014830.

Li, G., B. Ning, M. A. Abdu, Y. Otsuka, T. Yokoyama, M. Yamamoto, and L. Liu (2013), Longitudinal characteristics of spread F backscatter plumes observed with the EAR and Sanya VHF radar in Southeast Asia, J. Geophys. Res. Space Physics, 118, 6544–6557, doi:10.1002/jgra.50581.

Martinis, C. R., M. J. Mendillo, and J. Aarons (2005), Toward a synthesis of equatorial spread F onset and suppression during geomagnetic storms, J. Geophys. Res., 110, A07306, doi:10.1029/2003JA010362.

Ma, G., and T. Maruyama (2006), A super bubble detected by dense GPS network at east Asian longitudes, Geophys. Res. Lett., 33, L21103, doi:10.1029/2006GL027512.

Nishida, A. (1968), Coherence of geomagnetic DP 2 fluctuations with interplanetary magnetic variations, J. Geophys. Res., 73, 5549–5559, doi:10.1029/JA073i017p05549.

Otsuka, Y., K. Shiokawa, T. Ogawa, T. Yokoyama, M. Yamamoto, and S. Fukao (2004), Spatial relationship of equatorial plasma bubbles and field-aligned irregularities observed with an all-sky airglow imager and the Equatorial Atmosphere Radar, Geophys. Res. Lett., 31, L20802, doi:10.1029/2004GL020869.

Ott, E. (1978), Theory of Rayleigh-Taylor bubbles in the equatorial ionosphere, J. Geophys. Res., 83, 2066.

Patra, A. K., P. Srinivasulu, P. P. Chaitanya, M. D. Rao, and A. Jayaraman (2014), First results on low-latitude E and F region irregularities obtained using the Gadanki Ionospheric Radar Interferometer, J. Geophys. Res. Space Physics, 119, 10,276–10,293, doi:10.1002/2014JA020604.

Patra, A. K., P. P. Chaitanya, N. Dashora, M. Sivakandan, and A. Taori (2016), Highly localized unique electrodynamics and plasma irregularities linked with the 17 March 2015 severe magnetic storm observed using multitechnique common-volume observations from Gadanki, India, J. Geophys. Res. Space Physics, 121, 11,518–11,527, doi:10.1002/2016JA023384.

Pi, X., A. J. Mannucci, U. J. Lindqwister, and C. M. Ho (1997), Monitoring of global ionospheric irregularities using the worldwide GPS network, Geophy. Res. Lett., 24(18), 2283–2286.

Rajesh, P. K., C. H. Lin, C. H. Chen, J. T. Lin, T. Matsuo, M. Y. Chou, W. H. Chen, M. T. Chang, and C. F. You (2017), Equatorial plasma bubble generation/inhibition during 2015 St. Patrick's Day storm, Space Weather, 15, 1141–1150,

Rastogi, R. G. (1980). Seasonal variation of equatorial spread F in the American and Indian zones. Journal of Geophysical Research: Space Physics, 85(A2), 722-726.

Reinisch, B.W., J.L. Scali, D.L. Haines (1998). Ionospheric drift measurements with ionosondes. Ann. Geofis., 41, 695–702.

Reinisch, B. W., et al. (2009), New Digisonde for research and monitoring applications, Radio Sci., 44, RS0A24, doi:10.1029/2008RS004115.

Shen, C., Y. Chi, Y. Wang, M. Xu, and S. Wang (2017), Statistical comparison of the ICME's geoeffectiveness of different types and different solar phases from 1995 to 2014, J. Geophys. Res. Space Physics, 122, 5931–5948, doi:10.1002/2016JA023768.

Sobral, J. H. A., et al. (2009), Ionospheric zonal velocities at conjugate points over Brazil during the COPEX campaign: Experimental observations and theoretical validations, J. Geophys. Res., 114, A04309, doi:10.1029/2008JA013896.

Tsunoda, R. T. (1980), On the spatial relationship of 1-m equatorial spread F irregularities and plasma bubbles, J. Geophys. Res, 85, 185.

Tulasi Ram, S., P. V. S. Rama Rao, D. S. V. V. D. Prasad, K. Niranjan, S. Gopi Krishna, R. Sridharan, and S. Ravindran (2008), Local time dependent response of postsunset ESF during geomagnetic storms, J. Geophys. Res., 113, A07310, doi:10.1029/2007JA012922.

Wang, C. (2010), New Chains of Space Weather Monitoring Stations in China, Space Weather, 8, S08001, doi:10.1029/2010SW000603.

Wei, Y., et al. (2009), Westward ionospheric electric field perturbations on the dayside associated with substorm processes, J. Geophys. Res., 114, A12209, doi:10.1029/2009JA014445.

Woodman, R. F. (1970), Vertical drift velocities and east-west electric fields at the magnetic equator, J. Geophys. Res., 75(31), 6249–6259, doi:10.1029/JA075i031p06249.

Woodman, R. F., and C. LaHoz (1976), Radar observations of F region equatorial irregularities, J. Geophys. Res., 81(31), 5447–5461.

Woodman, R. F. (2009), Spread F—An old equatorial aeronomy problem finally resolved?. Ann. Geophys., 27, 1915–1934.

Yokoyama, T., S. Fukao, and M. Yamamoto (2004), Relationship of the onset of equatorial F region irregularities with the sunset terminator observed with the Equatorial Atmosphere Radar, Geophys. Res. Lett., 31, L24804, doi:10.1029/2004GL021529.

Yokoyama, T., and S. Fukao (2006), Upwelling backscatter plumes in growth phase of equatorial spread F observed with the Equatorial Atmosphere Radar, Geophys. Res. Lett., 33, L08104, doi:10.1029/2006GL025680.

Zhang, J.-C., R. A. Wolf, R. W. Spiro, G. M. Erickson, S. and Sazykin, F. R. Toffoletto, and J. Yang (2009), Rice Convection Model simulation of the substorm-associated injection of an observed plasma bubble into the inner magnetosphere: 2. Simulation results, J. Geophys. Res., 114, A08219, doi:10.1029/2009JA014131.
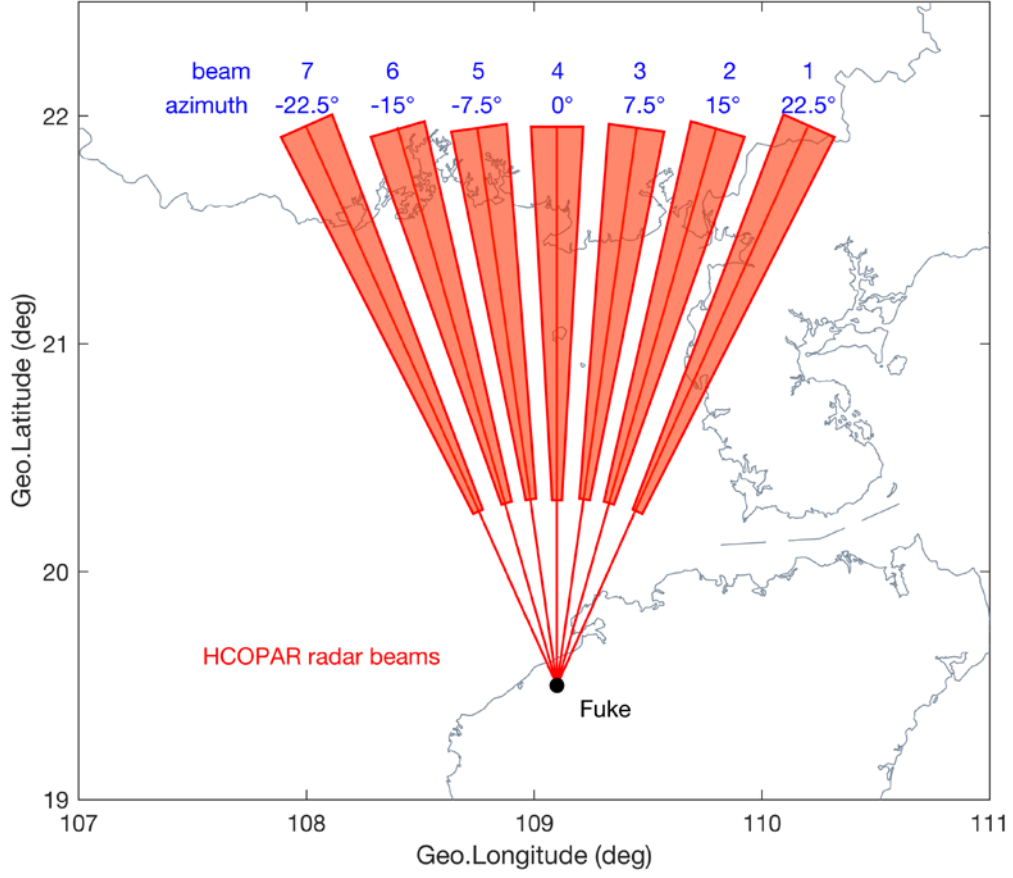
Figure 1. Map projection of the seven beam directions of HCOPAR. Each beam is separated by

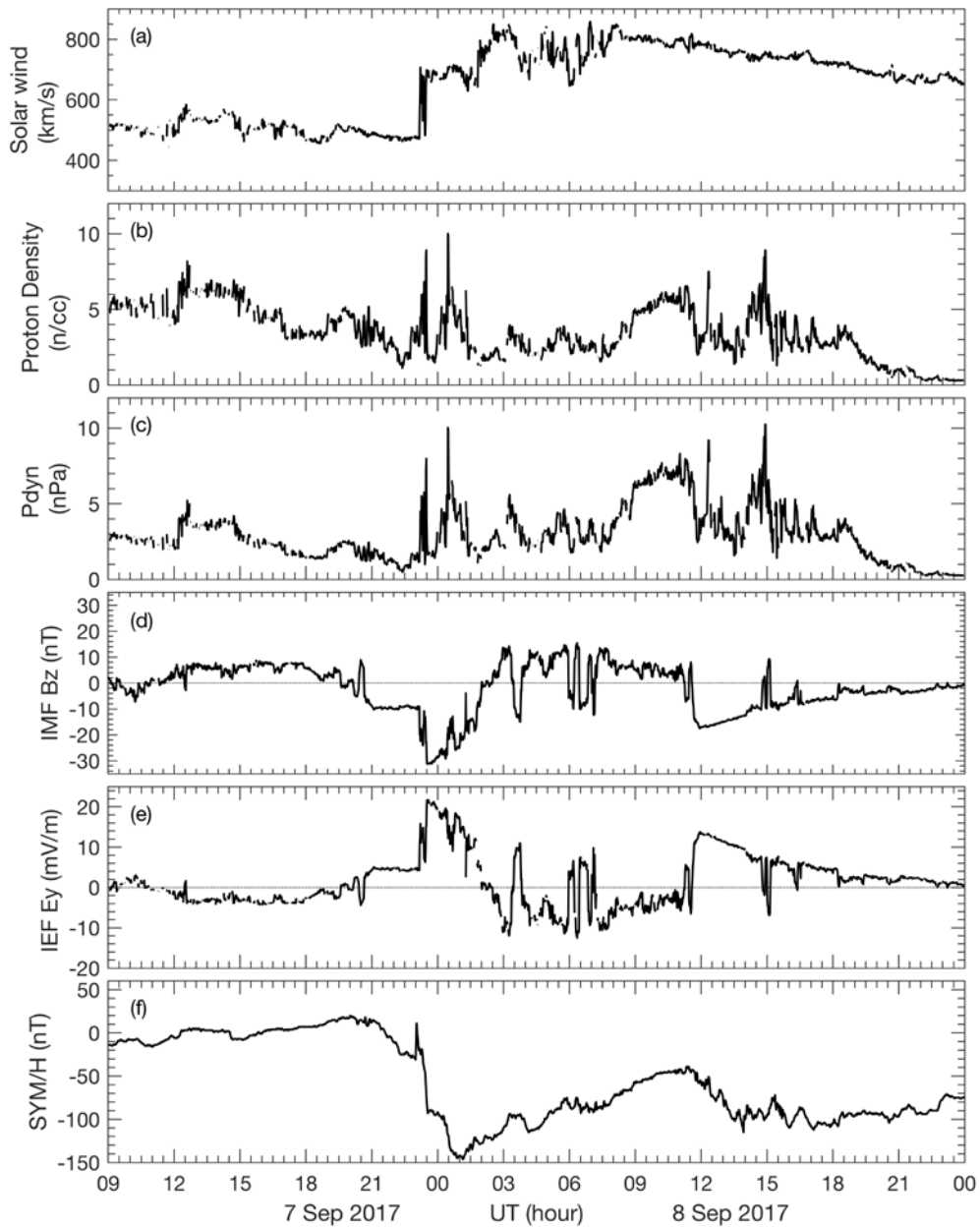7.5° in azimuth and beam 4 points to due geographic north.

Figure 2. Temporal variations of (a) solar wind velocity (km/s), (b) solar wind density (n/cc), (c)

solar wind dynamic pressure (nPa), (d) Z component of interplanetary magnetic field, IMF Bz

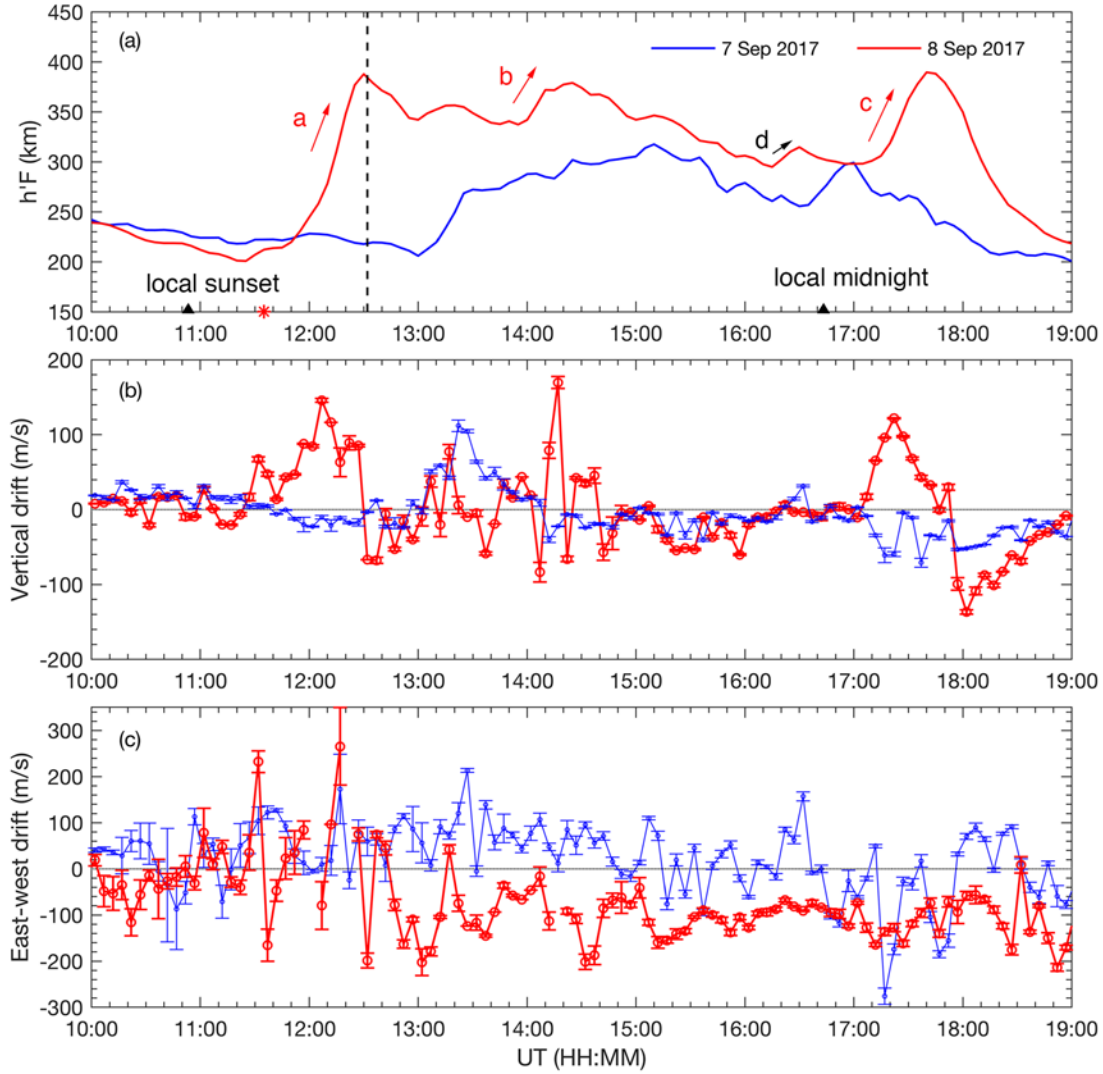(nT), (e) interplanetary electric field Ey component, IEF Ey (mV/m), and (f) the symmetric index, SYM/H index (nT) during 7-8 September 2017.

Figure 3. Time variations of (a) virtual height of bottom-side F layer, h'F (km), (b) vertical drift velocity of the F layer (m/s), and (c) east-west drift velocity of the F layer (m/s) observed by

Hainan digisonde on 7 (blue) and 8 (red) September 2017 during 10:00-19:00 UT. The red asterisk indicates the time when IEF Ey suddenly turned eastward. The vertical dashed line indicates the initial time of the FAIs observed by the HCOPAR. Local sunset and midnight are marked with two black triangles. Error bars represent the velocity spread.
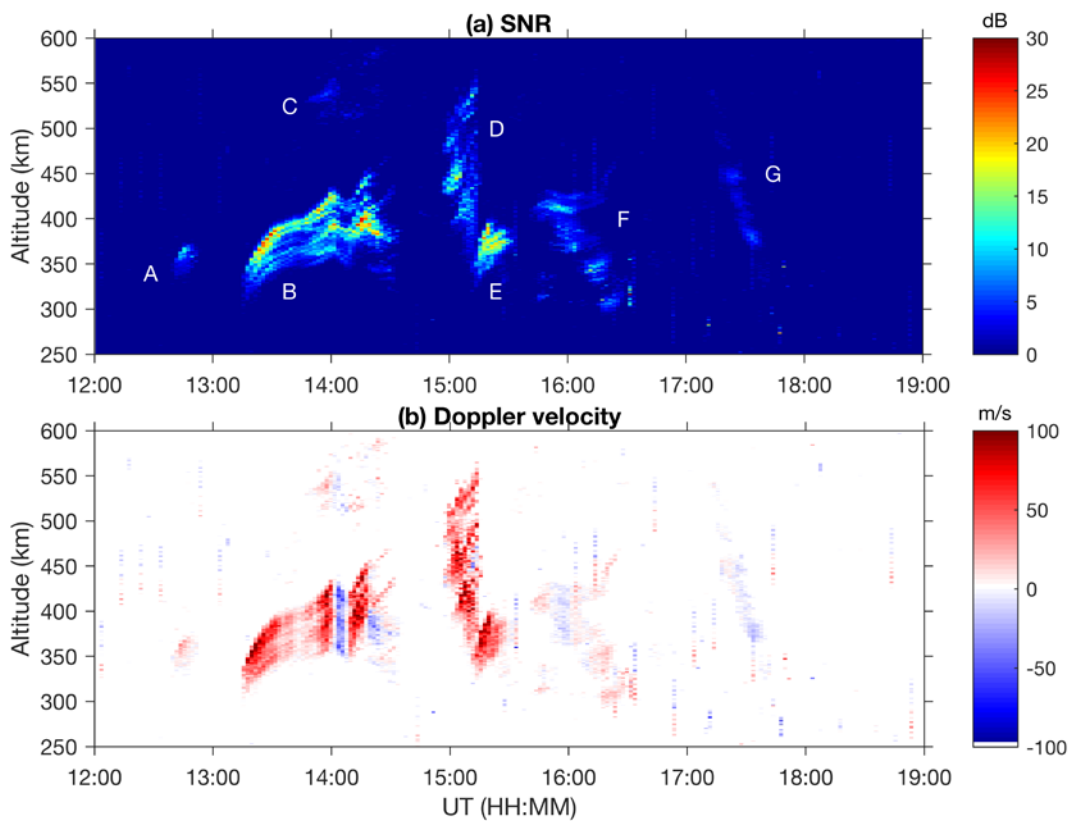

Figure 4. Altitude-time variations of (a) SNR (dB) and (b) line-of-sight Doppler velocity (m/s) of the FAIs observed on 8 September 2017 in beam 4 of the HCOPAR. Seven groups of FAIs are

labeled with A-G. Positive (negative) velocity represents the FAIs moving away (toward) the radar.
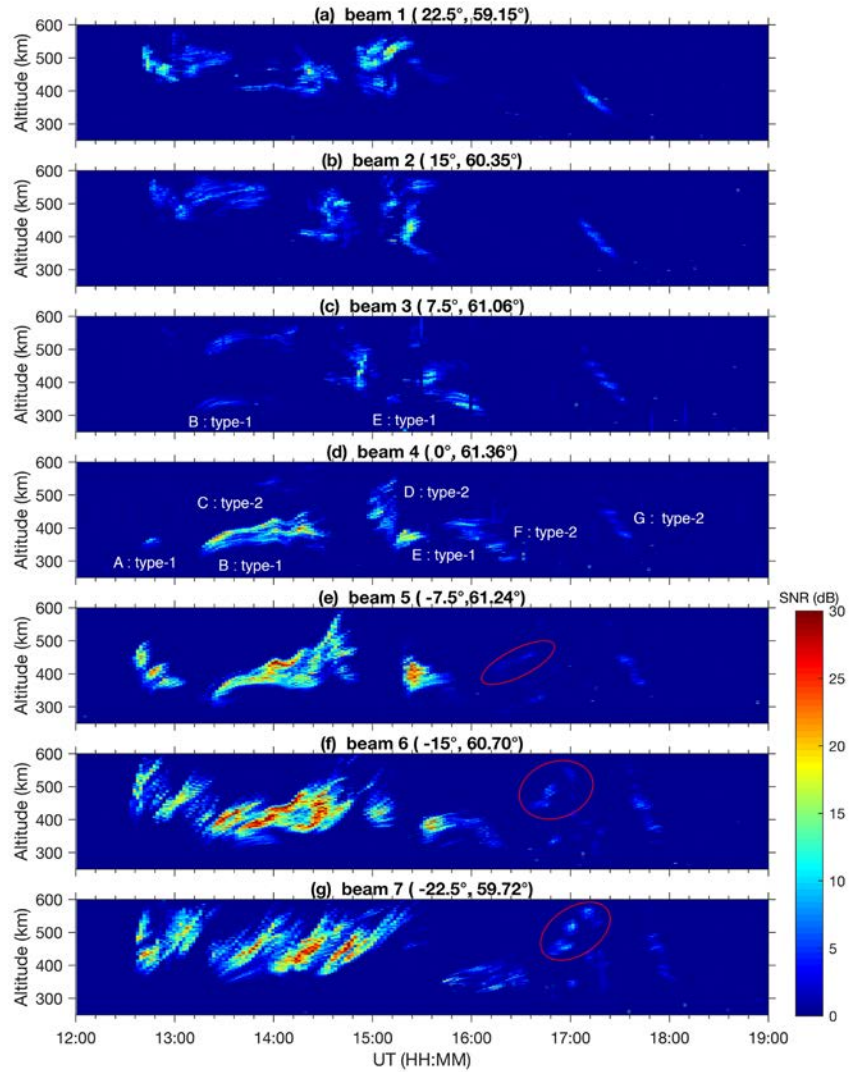
Figure 5. (a-g) Altitude-time-SNR plot of the FAIs echoes from different beam directions (between beam1 and beam7 at interval angle of 7.5°) from top to bottom. The groups A, B and E were freshly generated within the FoV of the radar and they are labeled as type-1 echoes. The groups C, D, F and G in beam 4 were firstly recorded by the easternmost beam, i.e. beam 1, and

they moved westward with decreasing echo intensity. These echoes are type-2 FAIs, which were generated further east of beam 1 and then drifted into the FoV of the radar.
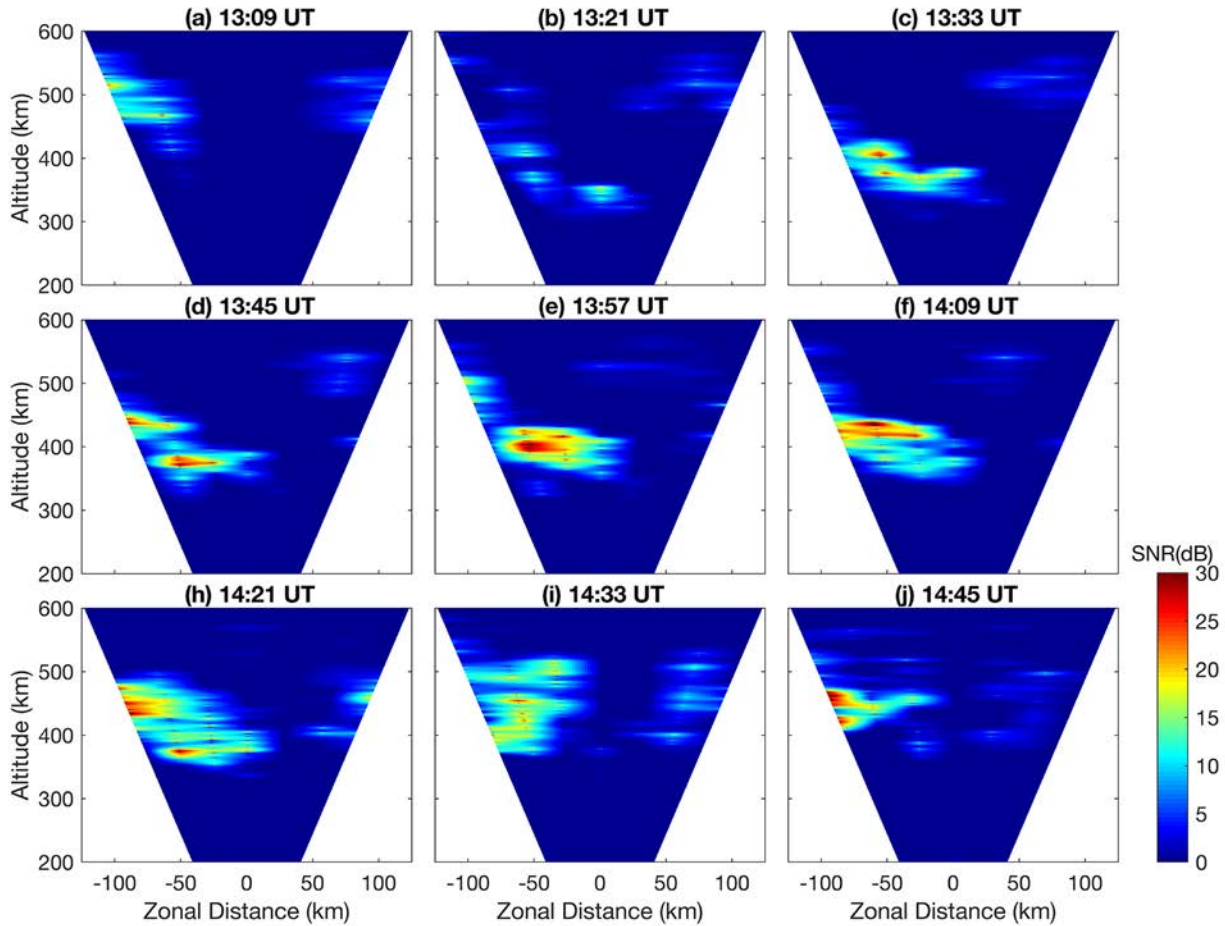

Figure 6. (a-j) Fan sector maps of the backscattered echo SNR in the zonal-vertical plane between 13:09 UT and 14:45 UT with a time step of 12 min on 8 September 2017 showing the

freshly generated type of the FAIs (group B in Figure 4a). The initiation can be seen in (b) near 300 km.
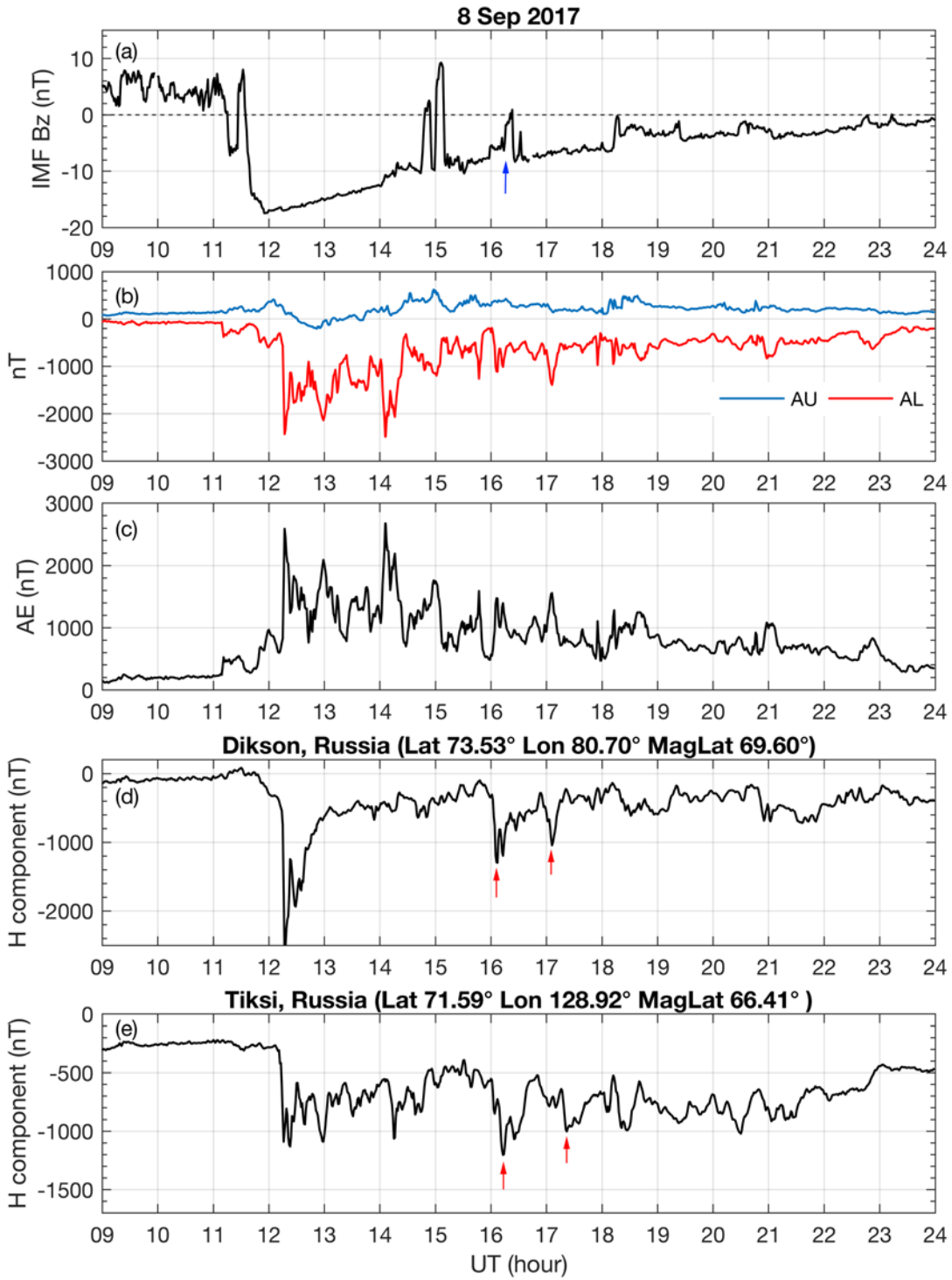
8 Sep 2017

Figure 7. (a) Zoomed in version of the IMF Bz (nT), (b) AU (blue) and AL(red) indices (nT), (c) AE index (nT), (d) H component (nT) at Dikson, Russia (73.53°N, 80.70°E, magnetic latitude 69.06°N), (e) H component (nT) at Tiksi, Russia (71.59°N, 128.92°E, magnetic latitude 66.41°N). Blue arrow in (a) indicates the short-period of IMF northward turning. Red arrows in (d) and (e) indicate the two consecutive substorm onsets.